OPEN ACCESS
Journal of Innovative Optical Health Sciences
Vol. 18, No. 6 (2025) 2550025 (15 pages)

DOI: 10.1142/S1793545825500257

World Scientific
www.worldscientific.com

Photoacoustic microscopy depth-of-field extension method and system based on three-dimensional continuity and sparsity deconvolution

Tingting Li*, Jialin Li*, Lingyu Ma*, Cheng Ma† and Mingjian Sun*,‡,§,¶

*Department of Control Science and Engineering, Harbin Institute of Technology
Harbin, Heilongjiang 150001, P. R. China

†Institute for Precision Healthcare, Tsinghua University
Beijing 100084, P. R. China

‡Department of Control Science and Engineering, Harbin Institute of Technology
Weihai, Shandong 264200, P. R. China

§Harbin Institute of Technology Suzhou Research Institute
Suzhou 215000, P. R. China
¶sunmingjian@hit.edu.cn

Received 6 April 2025
Accepted 28 May 2025
Published 10 July 2025

Optical-resolution photoacoustic microscopy is a novel imaging technique that combines the advantages of optical and ultrasound imaging, enabling high-resolution visualization of biological tissues at the micrometer scale. However, the divergence of the excited Gaussian beam limits the depth-of-field of the system to less than 100 μm, which hinders accurate three-dimensional imaging of living tissues and restricts its applicability in biological research. Therefore, there is an urgent need for an effective method to enhance the depth-of-field without altering the hardware configuration. This paper presents a photoacoustic microscopy depth-of-field extension method and system based on three-dimensional continuity and sparsity deconvolution. This method utilizes a depth-varying point spread function and incorporates continuity and sparsity constraints into the deconvolution process to mitigate the effect of background noise, enhancing the stability and accuracy of the depth-of-field extension. Experimental results using tungsten wire phantoms suggest that the depth-of-field of system can be extended to 650 μm, which is 7.2 times greater than conventional system, while improving the resolution of the defocused region by an average factor of 3.5. Furthermore, experiments on zebrafish and nude mouse ears with irregular topologies demonstrate that the proposed method successfully overcomes image blurring and the loss of structural information due to limited depth-of-field. All the results suggest that the system

¶Corresponding author.

with higher lateral resolution and enhanced depth-of-field has significant potential for a wide range of practical biomedical applications.

Keywords: Photoacoustic microscopy; depth-of-field extension; deconvolution.

1. Introduction

Optical-resolution photoacoustic microscopy (OR-PAM) is an emerging noninvasive medical imaging technology, that enables high-resolution visualization of biological tissues at the micrometer scale. It provides radiation-free imaging of microscopic structures, with applications in areas such as microvascular, brain, oral cavity, and bone tissue imaging.[1–5] In OR-PAM, a Gaussian beam, which can be focused to a micrometer-sized spot, is typically used to excite the photoacoustic signal. The light absorbers in the biological tissue absorb the laser energy and emit ultrasound through the thermoelastic effect under thermal and pressure constraints. The system captures the temporal data of each ultrasound wave via *A*-line scanning and subsequently performs two-dimensional raster scanning to generate three-dimensional images with depth information.[6–8] However, due to the diffraction of light, the Gaussian beam rapidly diverges along its propagation path, causing the spot size to expand outside the focal plane. This results in a limited depth-of-field (DOF) in OR-PAM, which makes it challenging to obtain three-dimensional images with consistent lateral resolution along the depth axis. The signal-to-noise ratio decreases in out-of-focus regions, leading to inaccurate structural information and limiting the clinical applicability of OR-PAM.[9–11] Therefore, it is crucial to enhance the DOF and improve lateral resolution in out-of-focus regions to achieve accurate structural imaging at different depths.

Several strategies have been proposed to extend the DOF of OR-PAM. Common techniques include Bessel beams, axial mechanical scanning, electronically controlled zoom lenses, and deep learning methods.[12] Bessel beams, which do not diffract during transmission and maintain their focusing properties over longer distances, have been used in optical and photoacoustic microscopy to extend the DOF. However, the side lobes of Bessel beams can illuminate nonrelevant regions, causing significant artifacts.[13–15] Axial mechanical scanning can achieve two-dimensional raster scanning at different depths by incorporating a vertically oriented motorized stage. However, it requires iterative updates to the focusing process, which increases system complexity.[16,17] Electronically controlled zoom lenses can rapidly adjust the focus position and focal length by applying voltage, optimizing the focus of the region of interest. However, the focusing speed is often insufficient to match the repetition frequency of optoacoustic pulsed lasers, limiting imaging speed.[18,19] Deep learning methods can extend the DOF without complex mechanical components by integrating physical principles for automatic data analysis. However, the limited availability of photoacoustic datasets and issues such as data drift can lead to poor model performance on unseen data, restricting their practical applicability.[20–22] Some studies have proposed enhanced photoacoustic microscopy strategies based on system modeling and data processing. These approaches show strong potential for improving image quality, enhancing contrast, and identifying functional features.[23–26] However, most of them focus on improving lateral resolution and do not address image degradation in out-of-focus regions.

Deconvolution algorithms have been widely used in fluorescence microscopy, optical coherence tomography, ultrasound imaging, and photoacoustic imaging.[27–30] These algorithms assume that image degradation can be modeled as the convolution of the original image with the point spread function (PSF) of the system. Deconvolution of photoacoustic images using the PSF can recover the original image at different depths.[31] In fluorescence microscopy and photoacoustic imaging, deconvolution has shown promise in improving spatial resolution, suppressing artifacts, and extending the DOF.[26,32,33] However, deconvolution is sensitive to noise, and it can converge to misleading solutions when noise is present, leading to instability in DOF extension.[34] Therefore, it remains a challenge to deconvolve three-dimensional OR-PAM data with noise while improving lateral resolution in out-of-focus regions and stably

extending the DOF without increasing system costs or computational time.

In this paper, we introduce a three-dimensional continuity and sparsity deconvolution-based photoacoustic microscopy (CSD-PAM) method to extend the DOF. The method utilizes the PSF at different depths and incorporates two a priori knowledge constraints: the spatial continuity of biological tissue samples and the sparsity of high-frequency information. These constraints guide the iterative deconvolution process, which is based on the accelerated Nesterov alternating direction method of multipliers (AN-ADMM) combined with Richardson-Lucy deconvolution. This approach effectively recovers each degraded pixel in the photoacoustic image at various depths, mitigating the effects of noise and interference. To validate the method, we conducted experiments using tungsten phantoms, zebrafish, and nude mouse ears. The results suggest that the proposed method effectively addresses image blurring and information loss caused by limited DOF, providing a more efficient and stable solution for extending the DOF without increasing system costs.

2. Materials and Methods

2.1. *Theoretical mode*

Considering the diffusion of point sources in three-dimensional space due to light diffraction, the photoacoustic image obtained by OR-PAM can be modeled as the convolution of the original image with PSF at different depths. As a linear time-invariant system, the imaging process of the photoacoustic microscopy system can be expressed as

$$f(x,y,z) = p(x,y,z) * o(x,y,z) + n(x,y,z), \quad (1)$$

where $f(x,y,z)$ is the acquired three-dimensional OR-PAM image, $p(x,y,z)$ is the PSF of the OR-PAM system at different depths, $o(x,y,z)$ is the original image and $*$ is the convolution process. $n(x,y,z)$ is the noise term, which is estimated using the iterative wavelet transform method. The deconvolution method can mathematically recover the lost structural information of $o(x,y,z)$ in the out-of-focus region, thereby extending DOF.

Considering that traditional deconvolution methods are highly sensitive to noise, the continuity and sparsity constraints can be incorporated to obtain the OR-PAM image to be deconvolved, with a sufficiently high signal-to-noise ratio and preserved high-frequency information. This approach improves the stability of the deconvolution method, facilitating the recovery of the real image at different depths. The optimization function can be expressed as

$$\arg\min_{h(x,y,z)} \left(\frac{\lambda}{2} ||f(x,y,z) - h(x,y,z) - n(x,y,z)||_2^2 + R_{\text{Hessian}}(h(x,y,z)) + \lambda_{L1} ||h(x,y,z)||_1 \right), \quad (2)$$

where $h(x,y,z) = p(x,y,z) * o(x,y,z)$ is the convolutional image to be solved. The first term is the data fidelity term, with λ denoting the regularization parameter, which can be adjusted based on the noise level and the weight of the data fidelity term. The second term represents the continuity constraint, based on the prior knowledge that biological samples are spatially and temporally smooth, while noise exhibits discontinuities. The Hessian matrix regularization helps suppress noise while preserving the smoothness of structural features in OR-PAM. This is expressed as

$$\begin{aligned} R_{\text{Hessian}}(h) &= \left|\left| \begin{vmatrix} h_{xx} & h_{xy} & \sqrt{\lambda_1} h_{xz} \\ h_{yx} & h_{yy} & \sqrt{\lambda_1} h_{yz} \\ \sqrt{\lambda_1} h_{zx} & \sqrt{\lambda_1} h_{zy} & \lambda_1 h_{zz} \end{vmatrix} \right|\right|_1 \\ &= ||h_{xx}||_1 + ||h_{yy}||_1 + \lambda_1 ||h_{zz}||_1 + 2||h_{xy}||_1 \\ &\quad + 2\sqrt{\lambda_1} ||h_{xz}||_1 + 2\sqrt{\lambda_1} ||h_{yz}||_1, \end{aligned} \quad (3)$$

where $h_{xx}, h_{xy}, h_{xz}, \ldots$ is the gradient of the image in different directions, and λ_1 is used to adjust the weights of the Hessian term.

The third term is the sparsity constraint, with λ_{L1} used to adjust the sparsity. This constraint is based on the prior knowledge that the convolution with smaller PSFs generally results in sparse structures.[35] It efficiently extracts the high-frequency information by enforcing sparsity on both absolute and relative structures. Additionally, the combined continuity and sparsity constraints can mitigate the blurring of detail information during signal-to-noise ratio enhancement, ensuring that the to-be-deconvolved image approaches the ideal state. Figure 1 illustrates the architecture of the photoacoustic microscopy method based on three-dimensional continuity and sparsity deconvolution.

Equation (2) represents a convex optimization problem with two regularization terms (Hessian regularization and ℓ_1 regularization). To solve this problem, The AN-ADMM method, based on the plus accelerated Nesterov, is employed. This approach can enhance the processing of the constrained

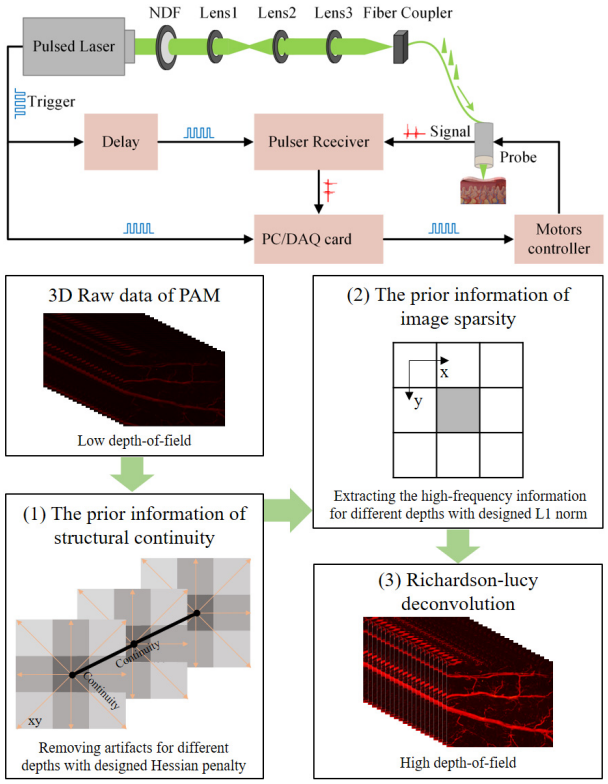

Fig. 1. Schematic diagram of CSD-PAM. NDF: neutral density filter; DAQ: data acquisition card; PC: personal computer.

optimization problem while enhancing both stability and convergence speed. The optimization function is constructed by introducing an auxiliary variable g:

$$\min_{h,g}\left(\frac{\lambda}{2}||f-h-n||_2^2+R_{\text{Hessian}}(h)+\lambda_{L1}||g||_1\right) \quad \text{subject to } g=h, \tag{4}$$

where f, h, n, and g are the abbreviations of $f(x,y,z)$, $h(x,y,z)$, $n(x,y,z)$, and $g(x,y,z)$, respectively. The optimization problem is then reconstructed based on augmented Lagrangian function:

$$L(h,j,u)=\frac{\lambda}{2}||f-h-n||_2^2+R_{\text{Hessian}}(h)+\lambda_{L1}||g||_1+\langle u,h-g\rangle+\frac{1}{2\rho}||h-g||_2^2, \tag{5}$$

where u is the dyadic variable and ρ is the penalty parameter. The principal variable h is optimized by fixing g and u, minimizing the augmented Lagrangian function pair h:

$$L(h,j,u)=\frac{\lambda}{2}||f-h-n||_2^2+R_{\text{Hessian}}(h)+\lambda_{L1}||g||_1+\langle u,h-g\rangle+\frac{1}{2\rho}||h-g||_2^2. \tag{6}$$

The AN-ADMM method introduces momentum during gradient updates to predict the current update direction and adjust the step size based on historical gradients. This approach enhances the efficiency of each update step, thereby accelerating the convergence process. The momentum term at each gradient update is calculated as

$$v^{k+1}=h^k+\beta(h^k-h^{k-1}), \tag{7}$$

where v^k is the acceleration step and represents the current h updated momentum. β is the Nesterov momentum factor. The update process is optimized based on the current momentum:

$$h^{k+1}=h^k-\alpha\nabla L(h^k,g^k), \tag{8}$$

where $\nabla L(h^k,g^k)$ is the gradient of the optimization function with respect to $h\cdot\alpha$ is the learning rate. Combined with accelerated Nesterov, it can provide an accelerated convergence mechanism while effectively avoiding the issue of falling into local optima that may occur with traditional gradient descent methods.

On this basis, the augmented Lagrangian function pair g is minimized by fixing h and u, and the auxiliary variable g is optimized:

$$g^{k+1}=\arg\min_g\left(\lambda_{L1}||g||_1+\frac{\rho}{2}||h^{k+1}-g+\frac{u^k}{\rho}||_2^2\right)\frac{1}{2}. \tag{9}$$

This is a standard soft-thresholding problem,[36] where the sparsity of the image can be achieved by forcing certain elements of g to become zero through a soft thresholding function:

$$g^{k+1}=\text{sign}\left(h^{k+1}+\frac{u^k}{\rho}\right)\cdot\max\left(0,\left|h^{k+1}+\frac{u^k}{\rho}\right|-\frac{\lambda_{L1}}{\rho}\right). \tag{10}$$

The pairwise variable u is then updated according to ADMM's standard update rules:

$$u^{k+1}=u^k+\rho(h^{k+1}-g^{k+1}). \tag{11}$$

Check that the difference between the primary variable h and the secondary variable g is sufficiently small:

$$||h^{k+1}-g^{k+1}||_2\le\varepsilon_{\text{prim}}, \tag{12}$$

where $\varepsilon_{\text{prim}}$ is the convergence threshold, and the iteration stops when the difference is small enough. The AN-ADMM method is able to maintain the stability and speed of solving continuity and

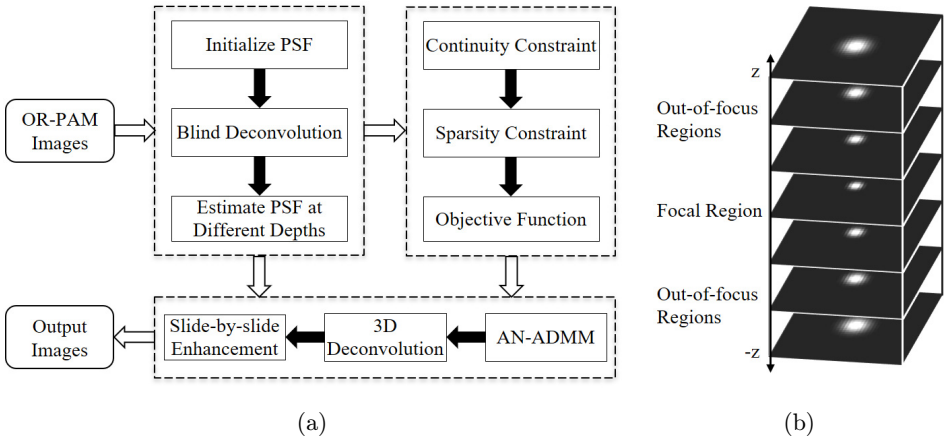

Fig. 2. The flow chart of the CSD-PAM: (a) workflow of the method; (b) depth-varying PSF.

sparsity-constrained problems, efficiently addressing complex optimization problems of OR-PAM.

Based on the image $h(x, y, z)$ to be deconvolved, which is solved by AN-ADMM and close to the ideal state, the application of the *R–L* deconvolution method can further address the issue of $h(x, y, z)$ missing structural information caused by light spot diffusion and enhances the spatial resolution at different depths. Each iteration updates the equation which can be rewritten as

$$o^{(k+1)}(x, y, z) = o^{(k)}(x, y, z) \cdot \left[\frac{h(x, y, z)}{p(x, y, z) * o^{(k)}(x, y, z)}\right], \quad (13)$$

Figure 2(a) illustrates flow chart of the CSD-PAM. Consider the diffuse distribution of point sources in space, which causes PSF inconsistency at different depths. In order to improve the image recovery accuracy in the out-of-focus region, the PSFs at various depths are flexibly updated using blind deconvolution. In the focal region, the PSF is constructed by measuring the actual resolution of the OR-PAM system, using the full width at half maxima of a Gaussian function. For out-of-focus regions, the initial PSF is used in the blind deconvolution process, which is applied to each off-focus layer to estimate PSFs at different depths. Specifically, the process begins with an initial Gaussian PSF and iteratively updates the PSF using a maximum likelihood estimation for each depth layer. Figure 2(b) presents the estimated PSFs at various imaging depths. It can be observed that the PSF in the focal region is relatively compact and symmetric, while the PSFs in out-of-focus regions show broadening. By introducing depth-varying PSF, accurate modeling of photoacoustic microscopy images can be achieved at different depths. Compared to using fixed PSFs, this PSF model enhances deconvolution accuracy and improves DOF extension without introducing significant artifacts. Using the above model CSD-PAM can recover an undegraded image along the depth direction, suppress the blurring problem of the original image caused by the expansion of the light spot, break through the diffraction limit of the system, and then obtain a three-dimensional large DOF photoacoustic microscopy image.

2.2. *Optical-resolution photoacoustic microscopy*

The photoacoustic microscopy proposed in this work comprises key modules: a coupled optical path module, a photoacoustic signal excitation module, a motion control module, a data acquisition and processing module, and a timing logic control module. The system can collect time data for each ultrasonic wave, and based on this, performs *B*-scanning to generate three-dimensional images. The system architecture is shown in Fig. 3.

To excite the photoacoustic signal, the system uses a 532 nm pulsed laser. The pulsed laser beam was attenuated by a neutral density filter (NDF) to control its intensity and then split into two separate paths by a beam splitter. One path was used to trigger a photodetector (PBS, PBS201, Thorlabs Inc., USA), which sent the signal to the host computer for triggering. The other path was spatially filtered by a mirror set consisting of lenses $L1$, $L2$ and diaphragm. This filtered beam is then coupled into a single-mode fiber using a fiber optic coupler

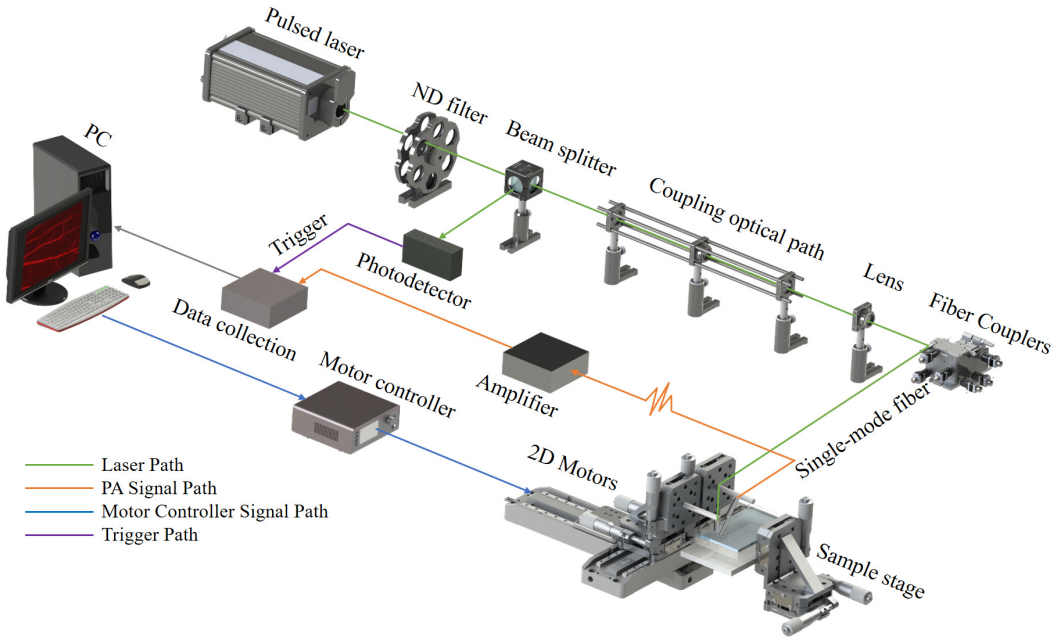

Fig. 3. Schematic diagram of optical-resolution photoacoustic microscopy.

(FC, PAF-X-7-A, Thorlabs Inc., USA), after which it is focused through a double gradient-index lenses probe for photoacoustic signal excitation. The effective numerical aperture of the probe is 0.21 by simulation. A custom-made needle hydrophone (center frequency: 50 MHz) was used to receive the PA signals, which were transmitted to the host computer through a signal amplifier. The photoacoustic signal excitation module was driven by a two-dimensional linear motorized stage (M-404, Physik Instrumente, Karlsruhe, Germany) for scanning to achieve photoacoustic microscopy. The overall hardware of photoacoustic microscopy is shown in Fig. 4.

The working sequence of the optical-resolution photoacoustic microscopy system based on a single-array element is shown in Fig. 5(a). The actual lateral resolution of the system has been calculated to be 3.75 μm, determined using the edge-to-edge method. First, a photoacoustic image of the sharp-edged blade is acquired, and the contour along the dashed line is extracted and fitted using the edge spread function (ESF). The line spread function (LSF) is then obtained by taking the derivative of the ESF. Finally, the lateral resolution is determined by measuring the full width at half maximum (FWHM) of the LSF (Fig. 5(b)). The theoretical lateral resolution is calculated to be 1.29 μm using the formula $0.51 \times \lambda/\mathrm{NA}$, where λ is the laser

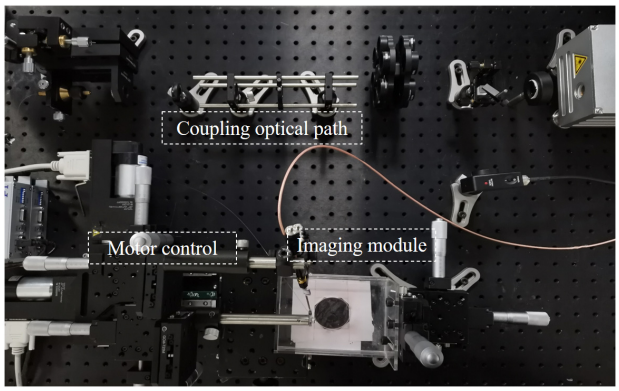

Fig. 4. The overall hardware of photoacoustic microscopy.

wavelength of 532 nm, and NA is the effective numerical aperture of the double gradient-index lenses probe, which is 0.21. The discrepancy between the actual and theoretical lateral resolution is likely due to light diffraction.

2.3. *Sample preparation and arrangement*

To evaluate the ability of CSD-PAM to perform three-dimensional imaging with an extended DOF, we constructed a phantom consisting of two tungsten filaments. The 250 μm tungsten filament was placed horizontally, while the 180 μm tungsten filament was positioned at an inclination of

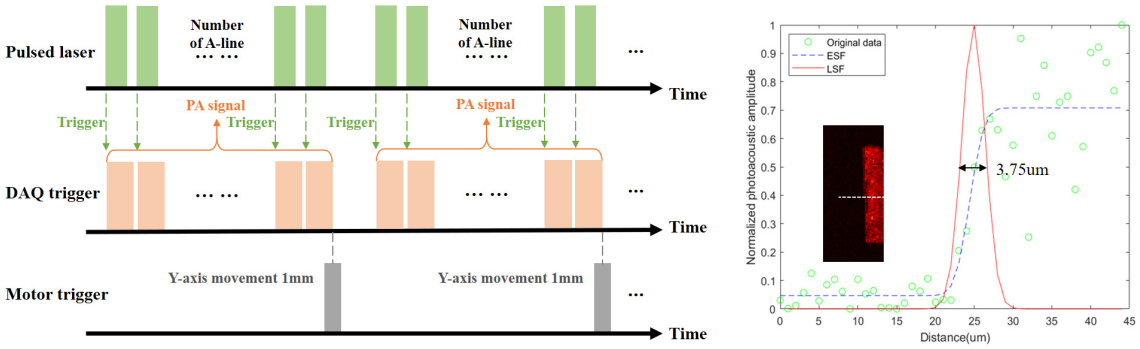

(a) (b)

Fig. 5. The working sequence and lateral resolution of photoacoustic microscopy: (a) working sequence of photoacoustic microscopy; (b) lateral resolution of photoacoustic microscopy.

approximately 5° along the depth direction. The imaging depth range of the two tungsten filaments spanned from 0 μm to 400 μm. The model was excited using a 532 nm pulsed laser to generate photoacoustic signals. During the scanning process, the step size during image acquisition was 2 μm in both lateral directions, covering an area of 8 mm × 4 mm. The height of the scanning stage was kept fixed, and the relative heights of the optical and acoustic probes were maintained to ensure consistent three-dimensional photoacoustic microscopy data.

Subsequently, we performed a photoacoustic microscopy experiment on adult zebrafish to assess the ability to image targets with irregular topological surfaces in three dimensions. Prior to experiment, adult zebrafish were anesthetized and fixed onto slides. During the experiment, the imaging coupling medium was deionized water, and the temperature was maintained at 25°C using a thermostatic water tank. The zebrafish were then scanned over a 12 mm ×4 mm area and imaged in three dimensions, in compliance with the American National Standards Institute (ANSI) safety standards.

Additionally, to validate the system's ability to conduct *in vivo* imaging, we conducted the experiment on the ears of 8-week-old balb/c-nu nude mouse. The protocols and handling of the animals had been approved by Harbin Institute of Technology. Before the experiment, the mouse was fixed onto a custom experimental platform and anesthetized using a small animal anesthesia system (R500IP, RWD, China) with vaporized isoflurane (1 L/min air and 0.75% isoflurane). The body temperature of the mouse was maintained at 37°C with a heating device. During the experiment, the mouse ear was placed on axially tilted slides, and ultrasound gel was applied between the ear and the water tank. A lateral step size of 2 μm was used during image acquisition, covering an area of 7 mm × 2 mm. The 532 nm laser energy distribution in the mouse ear was measured to be 20 mJ/cm^2, which is within the ANSI safety limits.

To ensure effective photoacoustic image restoration in the proposed CSD-PAM framework, the weights for the Hessian term λ_1 and the sparsity term λ_{L1} were empirically set to $\lambda_1 = 0.1$ and $\lambda_{L1} = 0.05$. These values were selected based on the system to balance noise suppression and detail preservation. When performing multi-layer deconvolution using the depth-varying PSF, the AN-ADMM algorithm is employed for optimization. The selection of iteration parameters has a significant impact on both convergence speed and restoration accuracy. Specifically, the initial penalty parameter is typically set to $\rho = 1$ to ensure stable convergence. The Nesterov momentum factor β is typically set to 0.9 based on empirical experience, which accelerates convergence while maintaining solution stability. The learning rate α is set to $\alpha = 0.001$, to enable accurate parameter updates for each depth region. The number of AN-ADMM iterations has a direct impact on the image enhancement. While increasing the number of iterations generally leads to improved image enhancement, the performance gain tends to saturate beyond a certain point. Therefore, the termination condition can ensure that the method achieves a balance between computational efficiency and image enhancement.

3. Results

3.1. *Depth-of-field enhancement based on tungsten filament phantom*

To assess the feasibility of CSD-PAM for DOF enhancement through imaging and quantitative analysis, experiments were conducted on tungsten phantoms at varying depths using the constructed photoacoustic microscopy system to acquire the original system images. Under consistent hardware configurations and parameters, the DOF of the tungsten data was extended using both the existing Richardson–Lucy algorithm (RLD-PAM) and the proposed method.[37] Figures 6(a)–6(c) show the maximum amplitude projection (MAP) views of the tungsten filaments phantom along the depth direction, representing the DOF enhancement imaging results of the original system, RLD-PAM, and CSD-PAM, respectively, for comparative analysis. In the original MAP image (Fig. 6(a)), the 260 μm tungsten filament at the focal plane has nearly identical diameters and intensities. However, the 180 μm tungsten filament tilted out of the focal plane is indistinguishable and exhibits a significant intensity difference, due to the limited DOF of system. Both RLD-PAM and CSD-PAM demonstrate DOF enhancement, but as illustrated in Fig. 6(b), RLD-PAM only recovers the tungsten filament intensity at certain depths, failing to fully resolve the image due to noise convergence. In contrast, Fig. 6(c) shows that CSD-PAM maintains consistent signal strength and structural information across the entire

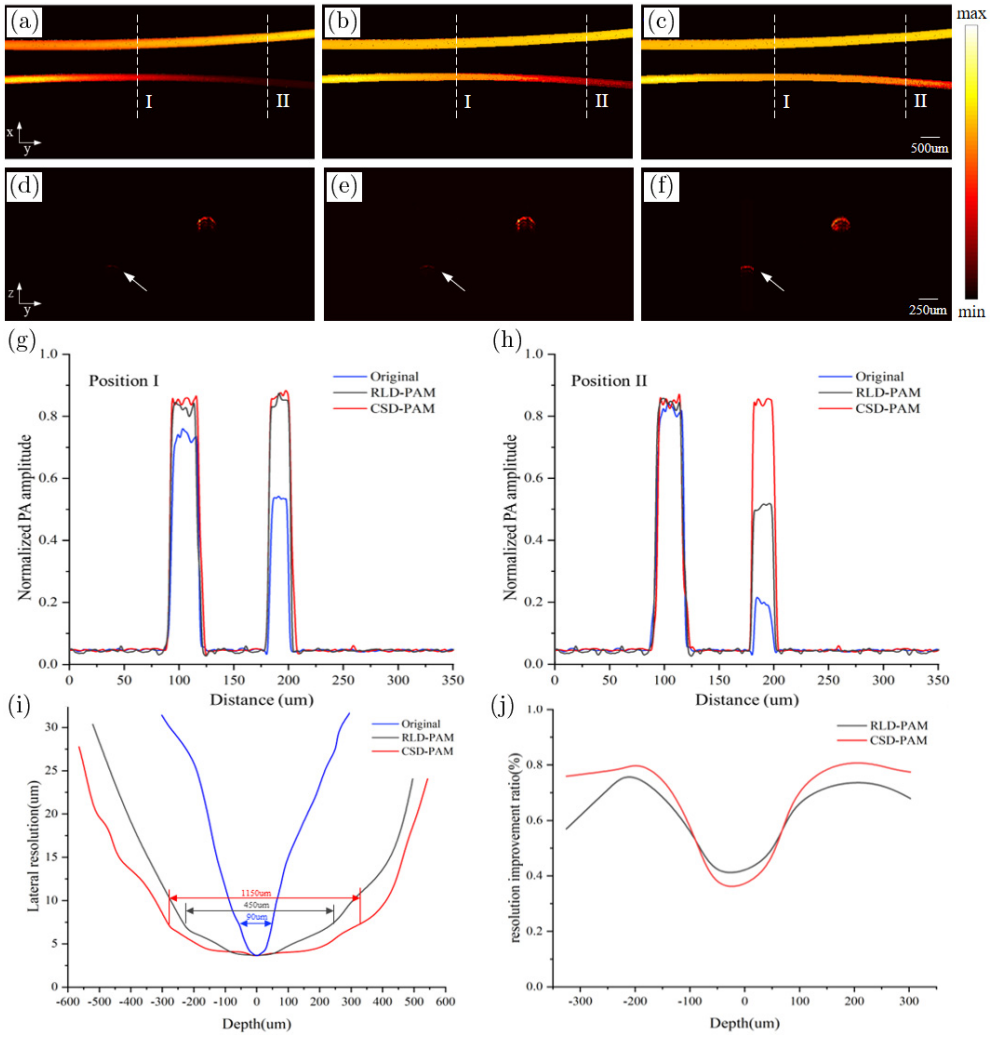

Fig. 6. Tungsten filaments phantom imaging: (a) original system image; (b) RLD-PAM image; (c) CSD-PAM image; (d)–(f) *B*-scan images corresponding to the dashed line II in (a)–(c), respectively; (g) and (h) line profiles corresponding to positions I and II in (a)–(c); (i) DOF of the systems; (j) resolution improvement ratio of the systems.

imaging depth, demonstrating a greater DOF. Figures 6(d)–6(f) provide the B-scan images corresponding to the dashed II position in Figs. 6(a)–6(c), further validating the imaging capability of the proposed method in the out-of-focus region. As indicated by the arrows, compared to the original B-mode image (Fig. 6(d)) and the RLD-PAM image (Fig. 6(e)), the CSD-PAM image (Fig. 6(f)) preserves high lateral resolution up to approximately 300 μm from the focal plane, and accurately recovers depth information.

Figures 6(g) and 6(h) show line profiles along the dashed lines in Figs. 6(d)–6(f) at positions I and II for quantitative evaluation of the tungsten signals obtained by the original OR-PAM, RLD-PAM, and CSD-PAM. At position I ($\sim$150 μm from the focal plane), both RLD-PAM and CSD-PAM provide improved profiles with enhanced structural visibility. However, at position II ($\sim$300 μm from the focal plane), RLD-PAM fails to recover the lost information, while CSD-PAM successfully recovers a more accurate tungsten filament diameter, with a signal intensity approximately five times that of the out-of-focus position. This further demonstrates the superior ability of CSD-PAM to recover structural information in the out-of-focus region.

Figure 6(i) shows the lateral resolution values obtained using the edge-to-edge method against the distance from the focal plane to calculate the DOF of the system for the different methods. Here, the DOF of a photoacoustic microscopy system is defined as the depth at which the lateral resolution increases to twice its minimum value.[38] The estimated DOF for the original system, RLD-PAM, and CSD-PAM were approximately 90 μm, 450 μm, and 650 μm, respectively. Figure 6(j) shows the relationship between the resolution improvement ratio and the distance from the focal point. The results indicate that CSD-PAM achieves superior resolution enhancement compared to RLD-PAM, particularly at positions farther from the focal plane. These results demonstrate that, while the lateral resolution decreases sharply in the out-of-focus region, precise structural imaging can be achieved at greater depths with the proposed method, which improves the lateral resolution of the defocused region by an average of 3.5 times and extends the DOF by a factor of 7.2 compared to the original system.

To verify the importance of modeling depth-varying PSF in out-of-focus regions, we conducted tungsten phantom experiment comparing the image performance. Multiple crossed tungsten wires with a diameter of approximately 10 μm were used as imaging targets. These were placed at the same out-of-focus plane, while all hardware parameters and algorithm constraints were consistent, with only the PSF being varied. Figures 7(a)–7(c) show the original system image, the image of fixed PSF, and the image of depth-varying PSF provided by the proposed CSD-PAM. In the original out-of-focus

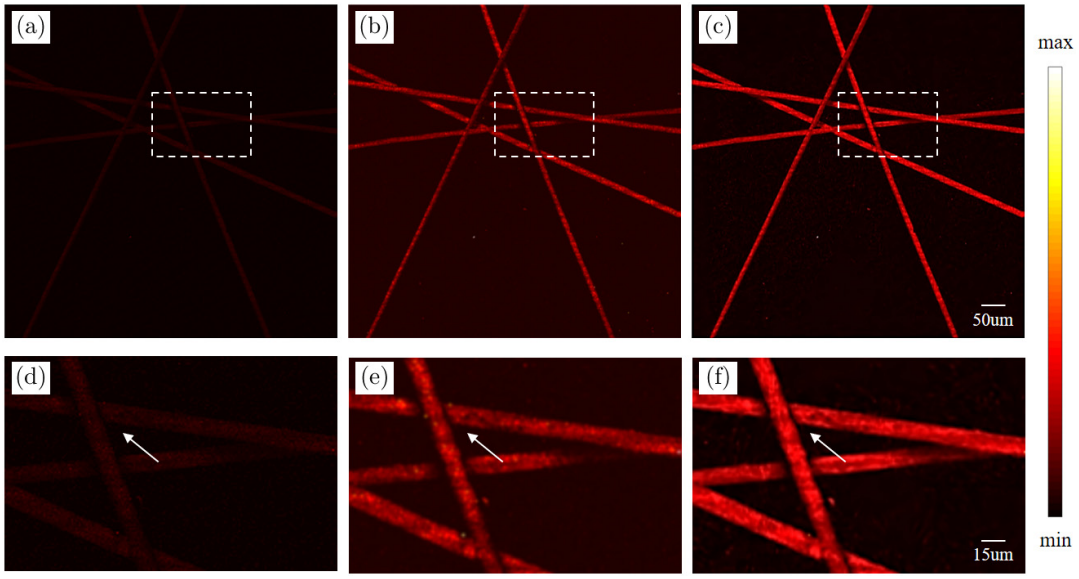

Fig. 7. Tungsten filaments phantom imaging: (a) original system image; (b) fixed PSF image; (c) depth-varying PSF image; (d)–(f) magnified regions of interest corresponding to the white boxes in (a)–(c).

image, the structural details of the tungsten wires are nearly indiscernible. While applying a fixed PSF for deconvolution, although some structure information can be recovered, it also introduces noise artifacts and signal loss, particularly at the boundary of the intersection region. It indicates that PSF mismatch can cause the algorithm to converge to the wrong solution. In contrast, the CSD-PAM significantly enhances the restored image quality. The obtained photoacoustic images provide clearer structural details and improved signal continuity, effectively mitigating artifacts and distortions caused by PSF mismatch. Figures 7(d)–7(f) further magnified the regions of interest corresponding to the white boxes in Figs. 7(a)–7(c), further illustrating the improvement. As indicated by the arrow positions, the CSD-PAM has significant advantages in texture continuity and structural realism.

To further quantitatively validate the advantages of the proposed in out-of-focus image restoration, we employed standard image quality evaluation metrics, including peak signal-to-noise ratio (PSNR) and structural similarity index (SSIM). The PSNR and SSIM of the CSD-PAM reached 39.55 dB and 0.9615 dB, significantly outperforming both the original system image and the fixed PSF image. These results indicate that the resolution of the out-of-focus region is significantly enhanced and almost restores the structural information of the tungsten wire. Overall, the above results demonstrate that depth-varying PSF modeling is essential for high-quality restoration photoacoustic microscopy images in out-of-focus regions, further verifying the effectiveness and superiority of the proposed CSD-PAM in extending the DOF (Table 1).

3.2. *Depth-of-field enhancement based on adult zebrafish in vivo*

To verify the advantages of CSD-PAM in imaging biological tissues with irregular surfaces and varying thicknesses, *in vivo* experiments were carried out on adult zebrafish, which have an uneven topology. Based on the strong light absorption by the surface pigmentation of adult zebrafish, excitation was performed using a 532 nm Gaussian beam to perform photoacoustic microscopy of the zebrafish cortex, which has millimeter-scale thickness, and to demonstrate the DOF enhancement provided by RLD-PAM and CSD-PAM.

Table 1. Evaluation metrics between enhancement images and raw image.

Compression ratio	PSNR	SSIM
Original image	32.62	0.8634
Fixed PSF	37.14	0.9303
Depth-varying PSF	39.55	0.9615

Figures 8(a)–8(c) show the original system, RLD-PAM and CSD-PAM acquired MAP images along the depth direction, respectively, for analyzing the performance of the imaging system through the outline structural information of the zebrafish. As shown in Fig. 8(a), at the focal plane, the original image presents the structural information of the head and pigmentation pattern of the body. However, in the tail out-of-focus region, the structural details of the body are nearly indistinguishable, which is due to the limited DOF of the system, compounded by the thickness of the zebrafish cortex. In contrast, as shown in Fig. 8(b), RLD-PAM enhances the signal at the focal plane but fails to fully recover the lost tail signal. This is due to its inability to effectively distinguish valid information in the presence of noise. However, in Fig. 8(c), CSD-PAM provides high-resolution head structure and fish body texture structure information of intact zebrafish, with clear margins and no significant difference in signal intensity. The method successfully recovers lost morphological details across different depths.

Figures 8(d)–8(l) zoom in on the regions of interest corresponding to the white boxes in Figs. 8(a)–8(c) to further analyze the texture details of the zebrafish. Compared to the blurred or even degraded original image, RLD-PAM is able to improve the resolution of the MAP image to some extent. In contrast, the extended DOF image obtained by CSD-PAM is able to extract information from the out-of-focus regions, showcasing richer, higher-resolution texture features with clearer and sharper fish body texture structure. The elliptical dashed lines in Figs. 8(d)–8(l) highlight the differences in imaging performance among the three methods. In typical out-of-focus regions, such as the tail vessels, body skin, and head skin, CSD-PAM produces images with clearer structural details and higher quality. These results demonstrate the effectiveness of CSD-PAM in imaging complex tissue structures. Figures 8(m)–8(o) show

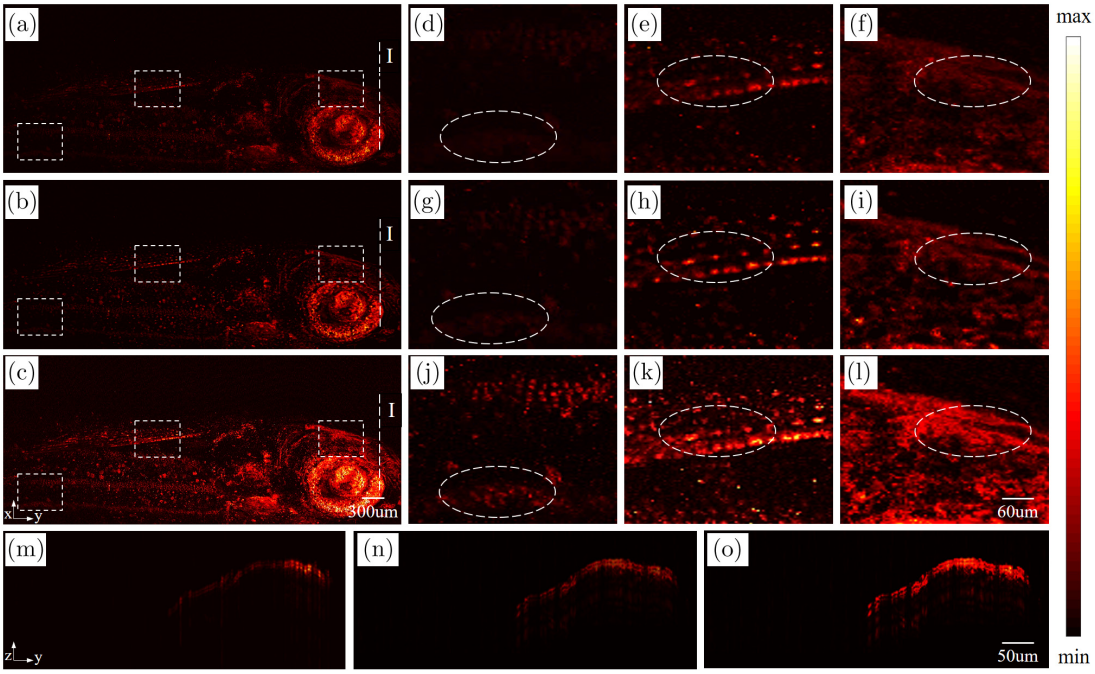

Fig. 8. Adult zebrafish imaging: (a) original system image; (b) RLD-PAM image; (c) CSD-PAM image; (d)–(f) magnified regions of interest corresponding to white boxes in (a); (g)–(i) magnified regions of interest corresponding to the white boxes in (b); (j)–(l) magnified regions of interest corresponding to white boxes in (b); (m)–(o) *B*-scan images corresponding to dashed I positions in (a)–(c).

the *B*-scan images corresponding to the dashed line I positions in Figs. 8(a)–8(c), respectively, further illustrating the depth information obtained from the zebrafish. These images demonstrate that the proposed method significantly improves the DOF of the system compared to the original and RLD-PAM images. Consistent photoacoustic signal intensity can be acquired at greater depths without the need for optical adjustments, demonstrating the superiority of CSD-PAM in imaging tissues with variable thicknesses and depth fluctuations.

3.3. *Depth-of-field enhancement based on mouse ear in vivo*

To better demonstrate the capability of CSD-PAM for large volume imaging and microvascular network analysis, experiments were conducted on tilted mouse ears to acquire as much axial information as possible for quantitative analysis.

To assess the value in microvascular network analysis, Figs. 9(a)–9(c) show the MAP images along the depth direction obtained by the original imaging, RLD-PAM, and CSD-PAM. As indicated by the arrow positions, CSD-PAM captures microvascular network with a higher and more stable signal-to-noise ratio, effectively suppressing noise and enhancing contrast compared to the original image and RLD-PAM. The results demonstrate that CSD-PAM achieves a greater DOF and more uniform spatial resolution. Figure 9(d) shows the acquired photoacoustic images at depths ranging from $-300\,\mu$m to $300\,\mu$m relative to the focal plane, based on the original system, RLD-PAM, and CSD-PAM, for analyzing the performance of the imaging system at different depths. In the original image, only the vessels within the focal plane are clearly distinguishable, while the vessels outside this region are blurred due to being out-of-focus. Compared to the original image, RLD-PAM recovered only part of the out-of-focus vessels at different depths but introduced significant clutter artifacts due to its convergence to a noise-dominated solution. As indicated by the arrows, the image obtained using the CSD-PAM method reveals a richer microvascular network, with tiny cortical vessels preserved. In contrast, the original image misses the micro vessels around the edges, and the RLD-PAM DOF extension method fails to produce high-quality photoacoustic images due to the presence of noise. Figures 9(e)–9(g) show zoomed-in views of the boxed area in Fig. 9(d), providing a clearer view to

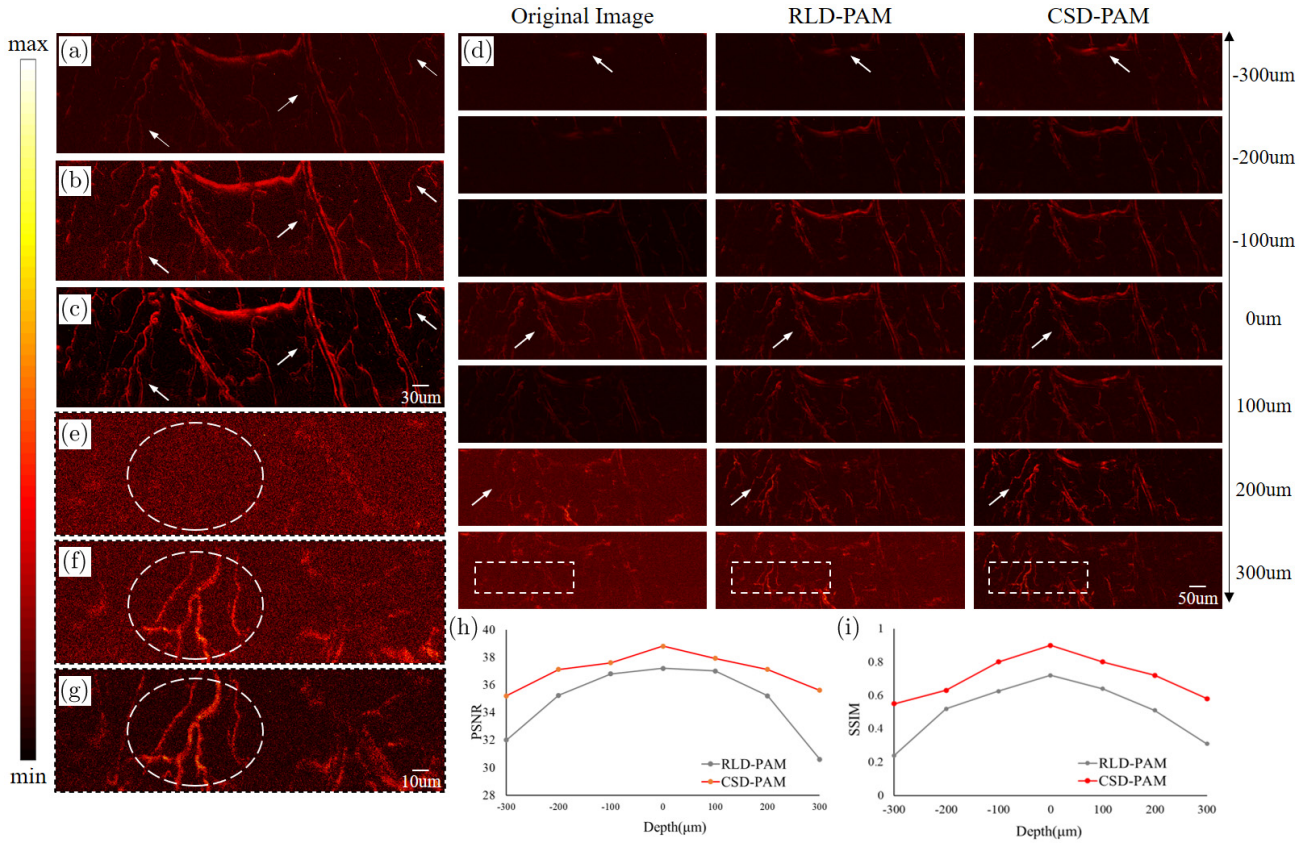

Fig. 9. Mouse ear imaging: (a) original system image; (b) RLD-PAM image; (c) CSD-PAM image; (d) the original system, RLD-PAM, and CSD-PAM images at depths from $-300\,\mu$m to $300\,\mu$m relative to the focal plane; (e)–(g) magnified regions of interest corresponding to white boxes in (d); (h) PSNR values along depth direction; (i) SSIM values along depth direction.

further analyze the detail resolution of the system. A detailed inspection of the circular framed regions reveals that, in out-of-focus regions, although weak signals are still detectable in the original image, the signal amplitude is mixed with background noise, resulting in the microvascular network structures being barely visible. Since image degradation can be modeled as the convolution of the original image with the PSF of system, RLD-PAM is able to partially restore the raw vascular signals and improve vascular clarity; however, it still exhibits noticeable background artifacts. In contrast, CSD-PAM effectively suppresses these artifacts by incorporating continuity and sparsity priors, accurately recovering more detailed vascular structure information in out-of-focus regions, even at $300\,\mu$m from the focal plane. The vessels are clearly distinguished from the background, which is superior to the RLD-PAM image, demonstrating the excellent performance of the method.

To quantitatively analyze the advantages of CSD-PAM, we compared the SSIM and PSNR along the depth direction for RLD-PAM and CSD-PAM images. The results are shown in Figs. 9(h) and 9(i), respectively. Over a depth range of $600\,\mu$m, CSD-PAM consistently outperforms RLD-PAM in terms of SSIM and PSNR. The SSIM of CSD-PAM images increases by an average of 55.04%. RLD-PAM performs better only in shallow out-of-focus regions, but as the blood vessels in the original images become blurred at deeper depths, the SSIM decreases rapidly. In contrast, CSD-PAM consistently recovers higher-quality micro vessels at various depths, maintaining relatively stable SSIM values. For PSNR, CSD-PAM achieves an average improvement of 16.92% in signal-to-noise ratio. The PSNR of the images decreases along the depth direction due to the rapid spreading of the Gaussian beam spot in out-of-focus regions. After processing with CSD-PAM, the PSNR decreases much more slowly, outperforming RLD-PAM, which experiences a rapid PSNR decay due to the lack of constraints. The background noise in the deeper out-of-focus regions is also significantly suppressed. These results

indicate that CSD-PAM is capable of capturing more detailed information about the vascular network structure stably, extending the DOF of the system for comprehensive analysis of the microvascular network.

After comprehensive qualitative and quantitative analysis of the tungsten filaments phantom, zebrafish, and vascular networks, it was found that, compared to the original system, CSD-PAM exhibits relatively consistent lateral resolution and stable performance in the depth direction. It effectively extends the DOF of system, showing potential value for a wide range of biomedical applications.

4. Discussion

OR-PAM is a noninvasive imaging technique that provides radiation-free, high-resolution images of microscopic biological tissues. It is widely used in the biomedical field. However, the Gaussian beam in OR-PAM rapidly diverges along its propagation path, resulting in a very limited DOF, typically only tens of microns. To achieve accurate three-dimensional imaging, an effective DOF extension method is needed. This paper presents a new method and system for extending the DOF in photoacoustic microscopy based on three-dimensional continuity and sparsity deconvolution. By modeling the system PSF at different depths, the optical properties of tissues at varying depths are more precisely described. The method incorporates two key prior knowledge constraints, spatial continuity and high-frequency sparsity, into the deconvolution process. A NA-ADMM algorithm based on accelerated Nesterov is used for the iterative solution, improving the accuracy of DOF extension and enabling clearer imaging in deep tissues. Both theoretical and experimental results validate these improvements. Tungsten filaments' phantom experiments demonstrated the feasibility of CSD-PAM for depth enhancement. Imaging and quantitative analysis showed that CSD-PAM successfully restored system images along the depth direction, extending the DOF to 650 μm. To further validate the advantages for biological tissues with uneven surfaces, live imaging of zebrafish and mouse ear was performed. Results showed that CSD-PAM overcame blur and information loss in out-of-focus areas, providing higher-quality images of the microvascular network in deep tissues. Although CSD-PAM performs well in DOF extension, it still has some limitations. Its performance depends on accurate estimation of the system PSF, and the corresponding PSF parameters must be recalculated for different photoacoustic systems to ensure effective deconvolution. Additionally, the computation time increases with image resolution and depth, which requires further optimization for real-time imaging applications. In conclusion, the proposed method and system show promising clinical application potential in photoacoustic imaging.

The CSD-PAM system proposed in this paper integrates several modules, including a coupling optical path module, a photoacoustic signal excitation module, a motion control module, a data acquisition and processing module, and a sequential logic control module. These modules work together to generate three-dimensional photoacoustic microscopy images. In terms of system architecture, a customized needle-shaped hydrophone with a center frequency of 50 MHz is used to achieve higher-resolution images. Additionally, a single wavelength of 532 nm is employed to better excite photoacoustic signals, which is particularly effective for hemoglobin imaging. In the future, the system's excitation source can be further enhanced to simultaneously capture multiple physiological parameters, such as blood oxygen saturation and metabolic changes. This would enable CSD-PAM to provide both functional imaging of oxygen levels and tissue metabolism, as well as precise structural imaging with a large depth of field, thus enhancing its biomedical application potential.

5. Conclusion

In this paper, we have developed a DOF enhancement method and photoacoustic microscopy system based on three-dimensional continuity and sparsity deconvolution. This method achieves a DOF extension of up to 650 μm. Compared to the traditional deconvolution method, the approach utilizing a depth-varying PSF for three-dimensional continuity and sparsity deconvolution effectively restores structural information in out-of-focus regions without increasing hardware costs. It overcomes the DOF limitation caused by the rapid divergence of Gaussian beams, while maintaining consistent lateral resolution, enhancing the stability of DOF extension and minimizing the impact of noise. Theoretical modeling, simulation experiments, and *in vivo* studies

demonstrate that the proposed method and system, CSD-PAM, can recover undegraded photoacoustic images along the depth direction, overcoming the issues of image blurring and structural information loss caused by optical path diffusion. Furthermore, it improves the lateral resolution and performance metrics of the system, improving the lateral resolution of the defocused region by an average of 3.5 times and extending DOF by up to 7.2 times compared to the original system. In addition to imaging zebrafish and mouse ears, the method holds great potential for applications in three-dimensional imaging of biological tissues with uneven surfaces, such as in studies evaluating the brain with curved cortex and the vascular network in tumors.

Acknowledgments

The research is supported by the National Key R&D Program of China [Grant No. 2022YFC2402400], the National Natural Science Foundation of China [Grant No. 62275062], Project of Shandong Innovation and Startup Community of High-end Medical Apparatus and Instruments [Grant Nos. 2023-SGTTXM-002 and 2024-SGTTXM-005], the Shandong Province Technology Innovation Guidance Plan (Central Leading Local Science and Technology Development Fund) [Grant No. YDZX2023115], the Taishan Scholar Special Funding Project of Shandong Province, and the Shandong Laboratory of Advanced Biomaterials and Medical Devices in Weihai [Grant No. ZL202402]. Tingting Li and Jialin Li are contributed equally to this work.

Conflicts of Interest

The authors declare that there are no conflicts of interest relevant to this paper.

ORCID

Tingting Li https://orcid.org/0009-0007-3216-5298
Jialin Li https://orcid.org/0000-0002-3165-9874
Lingyu Ma https://orcid.org/0000-0001-6050-5914
Cheng Ma https://orcid.org/0000-0001-7366-0091
Mingjian Sun https://orcid.org/0000-0001-8719-524X

References

1. X. W. Shen, H. P. Wu and L. Dong, "Recent advances of photoacoustic imaging technology in biomedicine," *Acta Photonica Sin.* **52**(3), 0352105 (2023).
2. Z. Xu *et al.*, "Visualising tumor angiogenesis and boundary with polygon-scanning multiscale photoacoustic microscopy," *Photoacoustics* **26**, 100342 (2022).
3. W. Qin *et al.*, "High-resolution *in vivo* imaging of rhesus cerebral cortex with ultrafast portable photoacoustic microscopy," *NeuroImage* **238**, 118260 (2021).
4. V. Periyasamy, M. Rangaraj and M. Pramanik, "Photoacoustic imaging of teeth for dentine imaging and enamel characterization," *Lasers in Dentistry XXIV*, Vol. 10473, pp. 42–47, SPIE (2018).
5. R. Cao *et al.*, "Label-free intraoperative histology of bone tissue via deep-learning-assisted ultraviolet photoacoustic microscopy," *Nat. Biomed. Eng.* **7**(2), 124–134 (2023).
6. J. W. Baik *et al.*, "Super wide-field photoacoustic microscopy of animals and humans *in vivo* ," *IEEE Trans. Med. Imaging* **39**(4), 975–984 (2019).
7. A. DiSpirito *et al.*, "Reconstructing undersampled photoacoustic microscopy images using deep learning," *IEEE Trans. Med. Imaging* **40**(2), 562–570 (2020).
8. C. Liu *et al.*, "Five-wavelength optical-resolution photoacoustic microscopy of blood and lymphatic vessels," *Adv. Photonics* **3**(1), 016002 (2021).
9. R. Cao *et al.*, "Optical-resolution photoacoustic microscopy with a needle-shaped beam," *Nat. Photonics* **17**(1), 89–95 (2023).
10. Y. Zhao *et al.*, "Ultraviolet metallens for photoacoustic microscopy with an elongated depth of focus," *Opt. Lett.* **48**(13), 3435–3438 (2023).
11. J. Ma *et al.*, "Transparent microfiber Fabry-Perot ultrasound sensor with needle-shaped focus for multiscale photoacoustic imaging," *Photoacoustics* **30**, 100482 (2023).
12. S. W. Cho *et al.*, "Sounding out the dynamics: A concise review of high-speed photoacoustic microscopy," *J. Biomed. Opt.* **29**(S1), S11521 (2024).
13. B. Park *et al.*, "Reflection-mode switchable subwavelength Bessel-beam and Gaussian-beam photoacoustic microscopy *in vivo* ," *J. Biophotonics* **12**(2), e201800215 (2019).
14. J. Yang *et al.*, "Motionless volumetric photoacoustic microscopy with spatially invariant resolution," *Nat. Commun.* **8**(1), 780 (2017).
15. Y. Hu *et al.*, "Extended depth-of-field all-optical photoacoustic microscopy with a dual non-diffracting Bessel beam," *Opt. Lett.* **44**(7), 1634–1637 (2019).

16. C. Yeh *et al.*, "Microvascular quantification based on contour-scanning photoacoustic microscopy," *J. Biomed. Opt.* **19**(9), 096011 (2014).
17. Z. Xu *et al.*, "Cortex-wide multiparametric photoacoustic microscopy based on real-time contour scanning," *Neurophotonics* **6**(3), 035012 (2019).
18. B. Li *et al.*, "*In vivo* fast variable focus photoacoustic microscopy using an electrically tunable lens," *Opt. Express* **22**(17), 20130–20137 (2014).
19. K. Lee *et al.*, "High-speed dual-layer scanning photoacoustic microscopy using focus tunable lens modulation at resonant frequency," *Opt. Express* **25**(22), 26427–26436 (2017).
20. R. Wang *et al.*, "Noise-insensitive defocused signal and resolution enhancement for optical-resolution photoacoustic microscopy via deep learning," *J. Biophotonics* **16**(10), e202300149 (2023).
21. Y. Zhou, N. Sun and S. Hu, "Deep learning-powered Bessel-beam multiparametric photoacoustic microscopy," *IEEE Trans. Med. Imaging* **41**(12), 3544–3551 (2022).
22. Y. Wu *et al.*, "Three-dimensional virtual refocusing of fluorescence microscopy images using deep learning," *Nat. Methods* **16**(12), 1323–1331 (2019).
23. H. Ma *et al.*, "Enhanced photoacoustic microscopy with physics-embedded degeneration learning," *Opto-Electron. Adv.* **8**(3), 240189-1–240189-19 (2024).
24. H. Ma *et al.*, "Monitoring of microvascular calcification by time-resolved photoacoustic microscopy," *Photoacoustics* **41**, 100664 (2025).
25. Y. Gao *et al.*, "4D spectral-spatial computational photoacoustic dermoscopy," *Photoacoustics* **34**, 100572 (2023).
26. T. Feng, H. Li and H. Ma, "Adaptively spatial PSF removal enables contrast enhancement for multilayer image fusion in photoacoustic microscopy," *Opt. Lett.* **49**(24), 7146–7149 (2024).
27. R. N. Zahreddine and C. J. Cogswell, "Total variation regularized deconvolution for extended depth of field microscopy," *Appl. Opt.* **54**(9), 2244–2254 (2015).
28. Z. Qiao, Y. Huang and Q. Hao, "Multi-shaping sparse-continuous reconstruction for an optical coherence tomography sidelobe suppression," *Opt. Lett.* **48**(21), 5679–5682 (2023).
29. X. Li *et al.*, "Deconvolution based on sparsity and continuity improves the quality of ultrasound image," *Comput. Biol. Med.* **169**, 107860 (2024).
30. L. Qi *et al.*, "Photoacoustic tomography image restoration with measured spatially variant point spread functions," *IEEE Trans. Med. Imaging* **40**(9), 2318–2328 (2021).
31. X. Huang *et al.*, "Fast, long-term, super-resolution imaging with Hessian structured illumination microscopy," *Nat. Biotechnol.* **36**(5), 451–459 (2018).
32. X. Zhang *et al.*, "Super-resolution reconstruction algorithm for optical-resolution photoacoustic microscopy images based on sparsity and deconvolution," *Opt. Express* **31**(1), 598–609 (2022).
33. B. Seong *et al.*, "E2E-BPF microscope: Extended depth-of-field microscopy using learning-based implementation of binary phase filter and image deconvolution," *Light Sci. Appl.* **12**(1), 269 (2023).
34. M. Laasmaa, M. Vendelin and P. Peterson, "Application of regularized Richardson-Lucy algorithm for deconvolution of confocal microscopy images," *Biophys. J.* **100**(3), 139a (2011).
35. W. Zhao *et al.*, "Sparse deconvolution improves the resolution of live-cell super-resolution fluorescence microscopy," *Nat. Biotechnol.* **40**(4), 606–617 (2022).
36. W. Deng, W. Yin and Y. Zhang, "Group sparse optimization by alternating direction method," *Wavelets and Sparsity XV*, Vol. 8858, pp. 242–256, SPIE (2013).
37. J. Chen *et al.*, "Blind-deconvolution optical-resolution photoacoustic microscopy *in vivo*," *Opt. Express* **21**(6), 7316–7327 (2013).
38. X. Song *et al.*, "High-resolution volumetric information fusion for depth of field enhancement in photoacoustic microscopy," *J. Biophotonics* **16**(3), e202200234 (2023).